Theoretical and Computational Acoustics'97
Y.-C. Teng, E.-C. Shang, Y.-H. Pao, M.H. Schultz, and A.D. Pierce (Editors)
© 1999 World Scientific Publishing Co.

Numerical Simulation of Sound Source Radiation in Flows

Christophe Bailly, Raphaël Thévenin, and Daniel Juvé
Laboratoire de Mécanique des Fluides et d'Acoustique,
Ecole Centrale de Lyon & UMR CNRS 5509,
BP 163, 6913 Ecully Cedex, France
E-mail: *bailly@selene.mecaflu.ec-lyon.fr*

The aim of this work is to develop a new solver for the Stochastic Noise Generation and Radiation (SNGR) model. This solver of the linearized Euler's equation is obtained by using a dispersion relation preserving (DRP) scheme in space combined with a fourth-order Runge-Kutta algorithm in time. The one-dimensional, linearized and full Euler's equations are integrated to test the numerical dispersion and dissipation properties of the solver. Some test cases from workshops in computational aeroacoustics are investigated. The two-dimensional linearized Euler equations are then solved with the same numerical algorithm, and the radiation boundary conditions of Tam & Webb are implemented. Finally, the case of an acoustic source in a sheared mean flow is computed and the numerical solution is compared to ray tracing and to the results predicted by the inviscid linear instability theory.

1 Introduction

The Stochastic Noise Generation and Radiation (SNGR) model is an alternative way to compute turbulent mixing noise[4,1,6]: Linearized Euler's equations are solved with a stochastic turbulent source term generated by a sum of random Fourier modes. As a consequence, all the mean flow effects are taken into account in the acoustic propagation,[2] and complex aeroacoustic configurations such as noise generated in a duct obstructed by a diaphragm can be treated.[3] The aim of this study is to improve the solver of the SNGR model. In the previous method a directional splitting was applied, and the one-dimensional solver was based on a weak formulation of the linearized Euler equations[10] in order to calculate two-dimensional and axisymmetric solutions. There are some difficulties in applying this formulation to a three-dimensional calculation.

In the present paper, the numerical solution of the linearized Euler's equations is obtained by using the 7-point stencil, dispersion relation preserving (DRP) scheme of Tam & Webb[13] in space

combined with a fourth order Runge-Kutta scheme in time. The second section describes the one-dimensional solver. The radiation of an acoustic source in a subsonic and a supersonic mean flow is then investigated in section 3. Section 4 deals with the full Euler's equations, which are integrated with the same space-time scheme, and a test case of a workshop in computational aeroacoustics[12] is studied. This method is then applied to the two-dimensional linearized Euler equations in section 5. Finally, the radiation of an acoustic source in a sheared mean flow is treated in section 6, and the numerical solution is compared to a ray-tracing.

2 One-dimensional solver

The one-dimensional Euler equations, linearized around a stationary mean flow, can be written as follows:

$$\frac{\partial \mathbf{U}}{\partial t} + \frac{\partial \mathbf{E}}{\partial x} + \mathbf{H} = \mathbf{S} \tag{1}$$

where $\mathbf{U}$ is the vector of unknows, $\mathbf{E}$ a flux vector and $\mathbf{H}$ a vector which is equal to zero when the mean flow is uniform:

$$\mathbf{U} = \begin{pmatrix} \rho' \\ \rho_o u' \\ p' \end{pmatrix} \quad \mathbf{E} = \begin{pmatrix} \rho' u_o + \rho_o u' \\ u_o \rho_o u' + p' \\ u_o p' + \gamma p_o u' \end{pmatrix} \quad \mathbf{H} = \begin{pmatrix} 0 \\ (\rho_o u' + \rho' u_o) \dfrac{\partial u_o}{\partial x} \\ (\gamma - 1) p' \dfrac{\partial u_o}{\partial x} - (\gamma - 1) u' \dfrac{\partial p_o}{\partial x} \end{pmatrix}$$

The density ρ', the velocity u' and the pressure p' designate small perturbations superimposed on a mean flow of density ρ_o, velocity u_o and pressure p_o. γ designates the ratio of specific heats, $\gamma = 1.4$ for air. The vector $\mathbf{S}$ represents possible unsteady sources. All the variables are nondimensionalized with the following scales: Δx for the length scale, c_o for the velocity scale, $\Delta x / c_o$ for the time scale, ρ_o for the density scale and $\rho_o c_o^2$ for the pressure scale, where Δx is the mesh step size and c_o the ambient sound speed. The 7-point DRP scheme of Tam & Webb[13] is used for the spatial discretization. The first derivative of any quantity f at the ith node of a uniform grid writes:

$$\left(\frac{\partial f}{\partial x}\right)_i \approx \sum_{j=-3}^{3} a_j f_{i+j} \tag{2}$$

The authors chose the coefficients[13,16] a_j of their spatial discretization by requiring that the wave number $\bar{k}$ provided by the finite difference scheme be a close approximation to the expected wave number. This optimized fourth-order scheme is better than a non-optimized sixth-order scheme using the same 7-point stencil. Figure 1 illustrates the characteristics of the DRP scheme in comparison with some standard central finite differences (CFD). Using the criterion $|k - \bar{k}| < 0.005$, the resolution for these schemes in terms of points per wavelength is:

CFD second-order	$k\Delta x \leq 0.30$	$\lambda/\Delta x \geq 21.3$
CFD fourth-order	$k\Delta x \leq 0.67$	$\lambda/\Delta x \geq 9.3$
CFD sixth-order	$k\Delta x \leq 0.96$	$\lambda/\Delta x \geq 6.6$
7-point DRP scheme	$k\Delta x \leq 1.16$	$\lambda/\Delta x \geq 5.4$

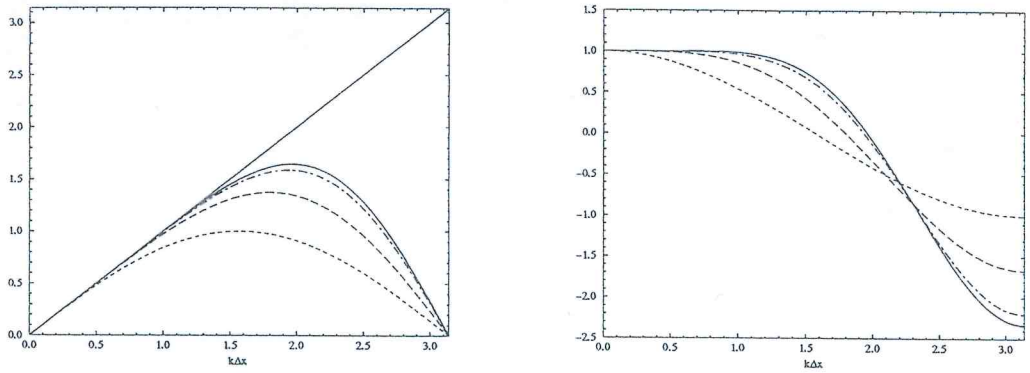

Figure 1: Wave number of the scheme $\bar{k}\Delta x$ as a function of the wave number $k\Delta x$, and $d\bar{k}/dk$ versus $k\Delta x$ for the DRP scheme of Tam & Webb ——, and some standard central difference schemes: - - - second-order, — — — fourth-order and — - — - sixth-order.

In some cases it is necessary to remove spurious numerical oscillations due to non linearities or mismatches with the boundary conditions, for instance. These short waves can be filtered by an artificial selective damping proposed by Tam & Shen.[14] For the system (1), the spatial discretization is then given by:

$$\frac{\partial \mathbf{U}_i}{\partial t} = -\sum_{j=-3}^{3} a_j \mathbf{E}_{i+j} - \frac{1}{R_s}\sum_{j=-3}^{3} d_j \mathbf{U}_{i+j} - \mathbf{H}_i + \mathbf{S}_i \tag{3}$$

where R_s is the mesh Reynolds number, which is usually taken on the interval [5 ; 10]. The notation $R_s = \infty$ will designate a calculation without artificial damping. The coefficients[14,16] d_j are chosen to damp only the short waves and not the long waves corresponding to an accurate resolution of the DRP scheme. The Fourier transform of the damping function collapses to the Gaussian function $\exp\left[-\ln 2\left((k\Delta x - \pi)/\sigma\right)^2\right]$ with a half-width of $\sigma = 0.2\pi$ for the linearized Euler's equation.

In this work we don't use the time advancement proposed by Tam & Webb[13] because of the low Courant-Friedrichs-Lewy (CFL) number corresponding to the stability limit, i.e. CFL ≤ 0.228 without mean flow. A four step Runge-Kutta algorithm is chosen for its high stability limit and its low storage requirement. The solution at time step $n+1$ is obtained by the following algorithm:

$$\begin{aligned}
\mathbf{U}_i^1 &= \mathbf{U}_i^n + \alpha_1 \Delta t \mathbf{K}_i^n \\
\mathbf{U}_i^2 &= \mathbf{U}_i^n + \alpha_2 \Delta t \mathbf{K}_i^1 \\
\mathbf{U}_i^3 &= \mathbf{U}_i^n + \alpha_3 \Delta t \mathbf{K}_i^2 \\
\mathbf{U}_i^{n+1} &= \mathbf{U}_i^n + \alpha_4 \Delta t \left(\mathbf{K}_i^3 + \mathbf{D}_i^n\right)
\end{aligned} \tag{4}$$

with:

$$\mathbf{K}_i^k = -\sum_{j=-3}^{3} a_j \mathbf{E}_{i+j}^k - \mathbf{H}_i^k + \mathbf{S}_i^k \quad \text{and} \quad \mathbf{D}_i^n = -\frac{1}{Rs}\sum_{j=-3}^{3} d_j \mathbf{U}_{i+j}^n$$

The coefficients α_i are chosen to obtain a fourth-order accuracy in time when the spatial operator is linear.[9] In this case, the stability limit corresponds to a CFL < 1.73, and the accuracy limit is CFL

< 0.73. Two other time integrations have been investigated, and a numerical result is given in the section dealing with nonlinear propagation.

The boundary conditions are very important in computation aeroacoustics[16] (CAA). Indeed, because of the high quality of the solver, any disturbance of small amplitude can be propagated in the computational domain, and the numerical solution is then contaminated. For the present applications, a linear version is implemented based on the general solution of the linearized Euler's equations[16]:

$$\mathrm{U} = F\left(\frac{x}{1+M} - t\right)\begin{pmatrix}1\\1\\1\end{pmatrix} + G\left(\frac{x}{M} - t\right)\begin{pmatrix}1\\0\\0\end{pmatrix} + H\left(\frac{x}{1-M} + t\right)\begin{pmatrix}1\\-1\\1\end{pmatrix} \tag{5}$$

where F, G and H represent respectively the outgoing acoustic wave, the entropy wave and the incoming acoustic wave. $M = U_o/c_o$ is the Mach number of the mean flow at the boundary of the computational domain. Two systems can be derived by differentiation[12] for the inflow condition and the outflow condition. The one-dimensional problem is easier to study since the velocity disturbance is purely of an acoustic nature.

3 Source radiation in one-dimensional flow

Several test problems can be found in the literature[12] to evaluate algorithms in CAA. We propose in this paper to compute the radiation of a source in a subsonic mean flow at $M = 0.5$ and in a supersonic mean flow at $M = 1.5$. The time step is $\Delta t = \mathrm{CFL}/(1+M)$ with a CFL number of 1 and a mesh Reynolds number $R_s = 10$. The source is implemented by using the vector S in equation (1) with:

$$\mathrm{S}(x,y) = 0.5\sin(\omega t)\, e^{-\alpha(x-x_s)^2}\begin{pmatrix}1\\0\\1\end{pmatrix}$$

where $\alpha = \ln(2)/9$. The source is located at $x_s = 200$ over the domain $0 \leq x \leq 400$ and its wavelength is $\lambda = 40$. In figure 2 the iso-contours of the pressure are plotted for the subsonic and the supersonic case. We can observe the two acoustic waves which propagate at the velocity $1 \pm M$ with an apparent wavelength $\lambda_c = (1 \pm M)\lambda$. Two profiles of the pressure are displayed in Figure 3 and are compared to the analytic solution derived from the elementary Green function given in appendix A. The two acoustic waves which propagate upstream and downstream in the subsonic case, and only downstream for the supersonic case, are calculated very accurately, without spurious oscillations near the source. The artificial selective damping is not necessary in subsonic flow but improves the results in supersonic conditions.

4 Nonlinear acoustic propagation

As suggested by Tam,[14,12] we use the same method to calculate the nonlinear wave propagation from the full Euler equations:

$$\frac{\partial \mathrm{U}}{\partial t} + \frac{\partial \mathrm{E}}{\partial x} = 0 \quad \text{with} \quad \mathrm{U} = \begin{pmatrix}\rho\\ \rho u\\ e_t\end{pmatrix} \quad \text{and} \quad \mathrm{E} = \begin{pmatrix}\rho u\\ \rho u^2 + p\\ u(e_t + p)\end{pmatrix} \tag{6}$$

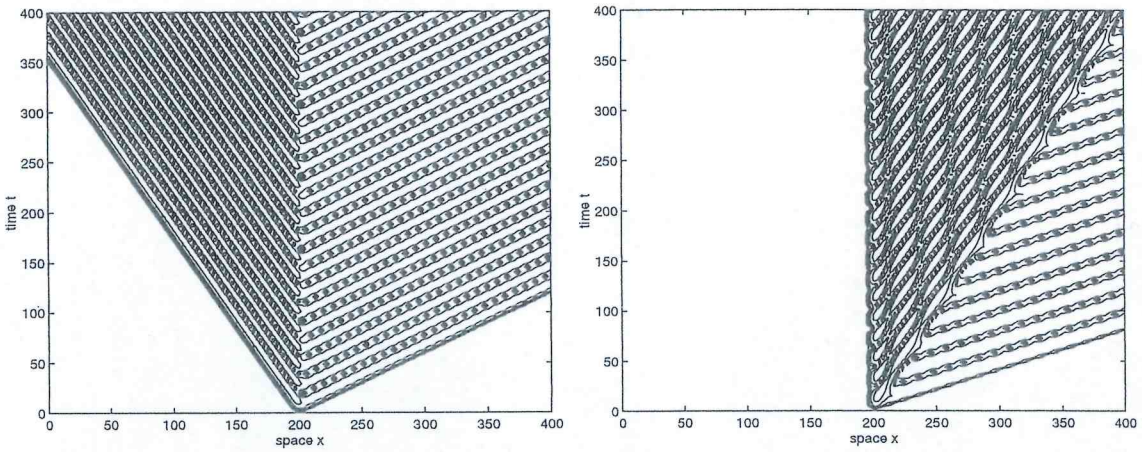

Figure 2: Source radiation in a subsonic and supersonic mean flow. Instantaneous contours of the logarithm of the pressure $\log_{10}|p|$, isolines from -1.4 to 0.2 (increment 0.4).

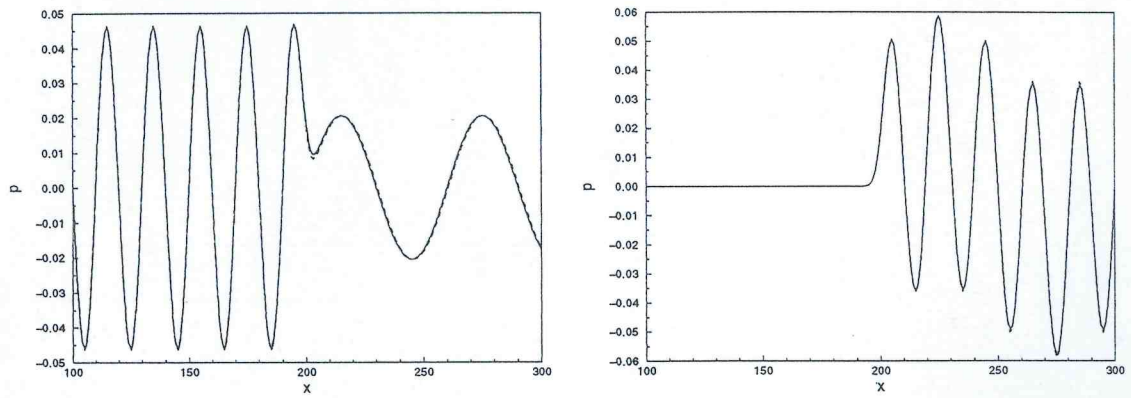

Figure 3: Profile of the pressure for source radiation in a mean subsonic flow at $M = 0.5$ and supersonic mean flow at $M = 1.5$. —— numerical solution, ----- analytical solution.

where the total specific energy is $e_t = \rho e + \rho u^2/2 = p/(\gamma - 1) + \rho u^2/2$ for a perfect gas. In the numerical integration, only the formulation of the damping is modified.[13] The mesh Reynolds number is now calculated as $R_s = u_s$ where $u_s = |u_{max} - u_{min}|$ is the difference between the maximum and the minimum velocity in the 7-point stencil. We use the value $R_s = 0.05$ as suggested by previous numerical studies.[16,8,12] This numerical integration is applied to the following initial value problem.[12] At time $t = 0$ the velocity profile is $u(x,0) = 0.5\exp(-\alpha x^2)$ with:

$$\rho = \left(1 + \frac{\gamma - 1}{2}\frac{u}{c_o}\right)^{\frac{2}{\gamma-1}} \qquad \text{and} \qquad p = \frac{1}{\gamma}\left(1 + \frac{\gamma - 1}{2}\frac{u}{c_o}\right)^{\frac{2\gamma}{\gamma-1}}$$

where $\alpha = \ln(2)/25$. An approximate analytical solution can be found by considering the simplified wave equation obtained by assuming isentropic fluctuations:

$$\frac{\partial u}{\partial t} + \left(1 + \frac{\gamma + 1}{2}u\right)\frac{\partial u}{\partial x} = 0$$

and by the use of Whitham's equal area rule[17,11] to determine the location of the shock. Figure 4 shows the evolution of the velocity in time. We observe the shock formation and at time $t = 200$, see Figure 5, the velocity profile is triangular in shape. The approximate analytical solution matches well with the calculated solution: As pointed out by Tam, the Whitham's method produces a shock at a slower velocity, and the numerical solution is usually more accurate. The artificial damping eliminates most of the oscillations near the leading edge. Three time algorithms have been used for this calculation[9]: the non optimized fourth-order, four-stages Runge Kutta scheme; the optimized sixth-order, six-stages Runge-Kutta scheme; and the optimized third-order; four-levels DRP scheme of Tam & Webb. The differences between these time integration schemes are too small to be noticed. However, a Runge-Kutta method requires a stability CFL number of 0.40 rather than 0.05 for the DRP scheme. The combination of the 7-point stencil DRP scheme in space with a standard fourth order Runge-Kutta algorithm in time seems an interesting compromise for computing linear and weakly nonlinear acoustic propagation based on its high stability CFL number, good accuracy and low storage.

5 Two-dimensional solver

We consider now the two-dimensional Euler equations linearized around a stationary mean flow. The components of the velocity are denoted $\mathbf{u} = (u, v)$ and the system corresponding to (1) is:

$$\frac{\partial \mathbf{U}}{\partial t} + \frac{\partial \mathbf{E}}{\partial x} + \frac{\partial \mathbf{F}}{\partial y} + \mathbf{H} = 0 \tag{7}$$

where the unknown vector $\mathbf{U}$ and the flux vectors $\mathbf{E}$ and $\mathbf{F}$ are written:

$$\mathbf{U} = \begin{pmatrix} \rho' \\ \rho_o u' \\ \rho_o v' \\ p' \end{pmatrix} \qquad \mathbf{E} = \begin{pmatrix} \rho' u_o + \rho_o u' \\ u_o \rho_o u' + p' \\ u_o \rho_o v' \\ u_o p' + \gamma p_o u' \end{pmatrix} \qquad \mathbf{F} = \begin{pmatrix} \rho' v_o + \rho_o v' \\ v_o \rho_o u' \\ v_o \rho_o v' + p' \\ v_o p' + \gamma p_o v' \end{pmatrix}$$

The vector $\mathbf{H}$ contains mean flow gradient terms, which are equal to zero when the mean flow is

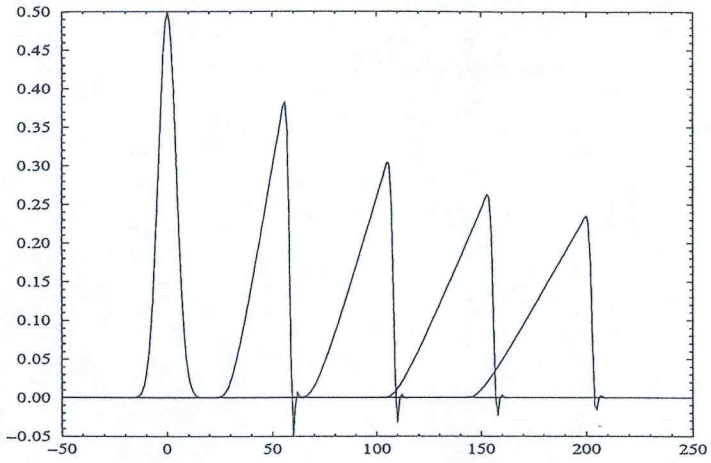

Figure 4: Evolution of the velocity at times $t = 0$, $t = 40$, $t = 80$, $t = 120$ and $t = 160$ with $R_s = 0.05$. —— fourth-order Runge-Kutta scheme (CFL=0.40), ----- sixth-order Runge-Kutta scheme (CFL=0.40).

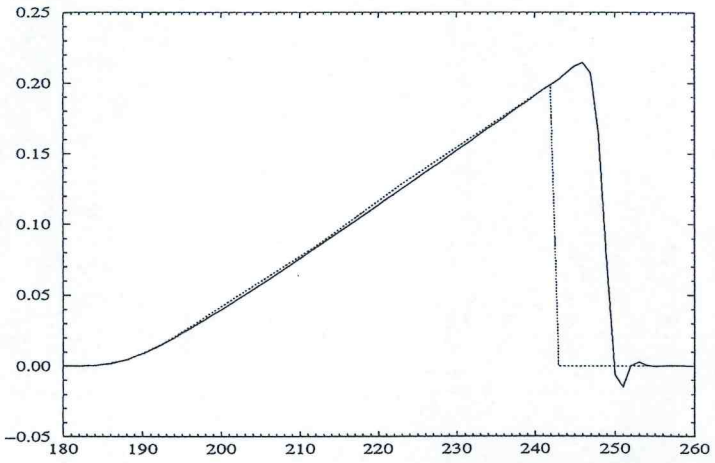

Figure 5: Velocity profile at time $t = 200$, with $R_s = 0.05$. —— fourth-order Runge-Kutta scheme (CFL=0.4), ----- optimized fourth-order, six-stages Runge-Kutta scheme (CFL=0.40), — - — - space-time DRP scheme (CFL=0.05). ····· approximate analytical solution.

uniform:

$$\mathbf{H} = \begin{pmatrix} 0 \\ (\rho_o u' + \rho' u_o)\dfrac{\partial u_o}{\partial x} + (\rho_o v' + \rho' v_o)\dfrac{\partial u_o}{\partial y} \\ (\rho_o u' + \rho' u_o)\dfrac{\partial v_o}{\partial x} + (\rho_o v' + \rho' v_o)\dfrac{\partial v_o}{\partial y} \\ (\gamma-1)\,p'\left(\dfrac{\partial u_o}{\partial x} + \dfrac{\partial v_o}{\partial y}\right) - (\gamma-1)\,u'\dfrac{\partial p_o}{\partial x} - (\gamma-1)\,v'\dfrac{\partial p_o}{\partial y} \end{pmatrix}$$

The computational method (4) is used with the following expressions for the spatial derivatives when the computational domain is discretized on a regular mesh:

$$\mathrm{K}^k_{i,j} = -\sum_{l=-3}^{3} a_l \left(\mathrm{E}^k_{i+l,j} + \mathrm{F}^k_{i,j+l}\right) - \mathrm{H}^k_{i,j} + \mathrm{S}^k_{i,j} \quad \text{and} \quad \mathrm{D}^n_{i,j} = -\frac{1}{Rs}\sum_{l=-3}^{3} d_l \left(\mathrm{U}^n_{i+l,j} + \mathrm{U}^n_{i,j+l}\right)$$

The boundary conditions of Tam and his colleagues[13,15] have been implemented. Without a mean flow, we use a radiation boundary condition for outgoing acoustic waves, based on an asymptotic solution of the linearized Euler's equations. For an outflow condition, the pressure disturbance is an acoustic fluctuation, which is not the case for the velocity and density disturbances. For these last two variables, Euler's equations are used.[13] Finally, a set of compatibility first-order differential equations is solved. To demonstrate the performance of the numerical method, the following initial value problem has been solved:

$$f(x, y, t=0) = \epsilon \exp\left[-\ln 2\,\frac{(x-x_s)^2 + (y-y_s)^2}{l}\right]$$

where the function f described the three initial perturbations:

perturbation f	ϵ	l	x_s	y_s
acoustic	0.01	9	0	0
entropic	0.001	25	33	33
vorticity	0.004	25	33	33

For the vorticity disturbance, the function f is the stream function. The mean flow at Mach $M = 0.5$ is in the direction of the diagonal of the computational domain: $-100 \leq x \leq 100$ and $-100 \leq y \leq 100$. Radiation boundary conditions are imposed at the bottom and left boundaries of the domain, and the outflow boundary conditions are applied to the two other sides of the domain. The density contours are plotted in Figure 6. The three perturbations arrive at the same time to the upper right-hand corner of the domain. The density profile along the diagonal line $x = y$ is plotted in Figure 7 for several times and for two values of the CFL number: CFL = 1 and CFL = 0.5. To get an accurate numerical result, the CFL number must be smaller to take into account the effective space step $\sqrt{2}\Delta x$ on the diagnonal line. In this last case, the difference between the exact solution[13,12] and the numerical one is less than 10^{-6}. There is no added damping in these calculations, i.e. $R_s = \infty$.

6 Source radiation in the Bickley jet

The two-dimensional solver of the linearized Euler equations is applied to calculate the source radiation in a sheared mean flow. We use the Bickley jet for the mean axial velocity:

$$\frac{u_o(y)}{u_{axe}} = \frac{1}{\cosh^2 \tilde{y}} \tag{8}$$

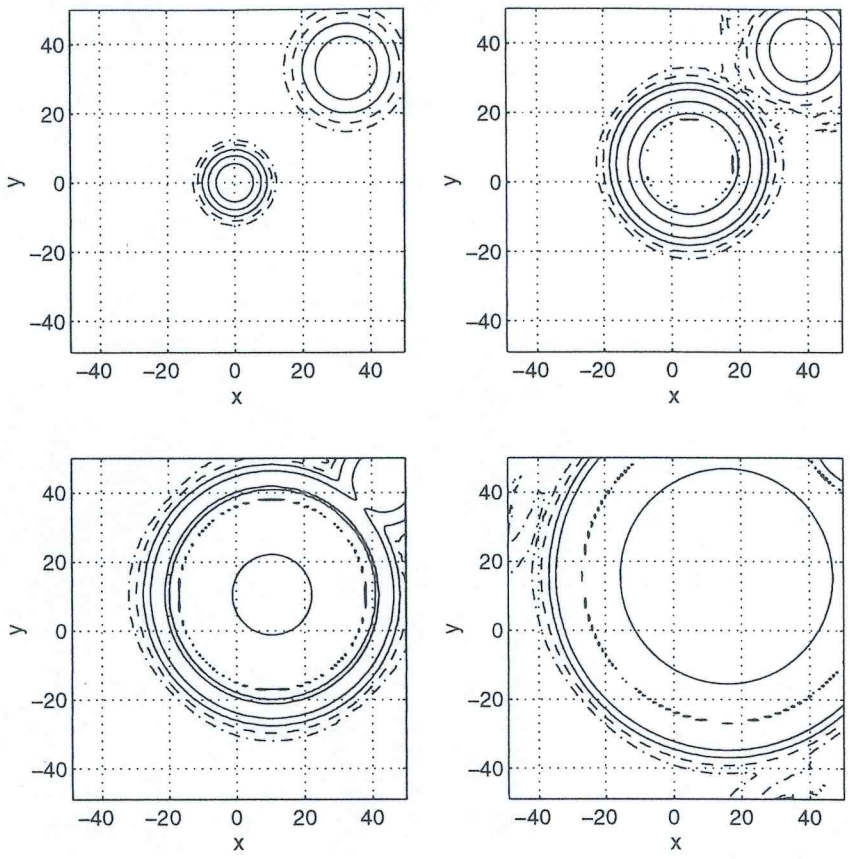

Figure 6: Iso-contours of the density at times $t = 0$, $t = 20$, $t = 40$ and $t = 60$. —— isolines 10^{-2}, 10^{-3}, 10^{-4}, 10^{-5}. ----- isoline 10^{-6}. — - — - isoline 10^{-7}.

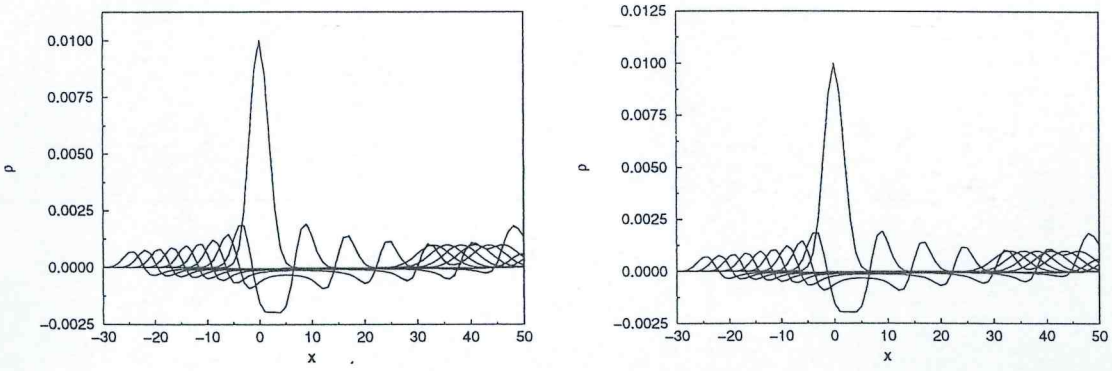

Figure 7: Profiles of the density along the line $x = y$, there is a time interval of 10 between each profile. —— numerical solution, ----- exact solution. The left and right figures correspond to a numerical solution with a CFL number of 1 and 0.5, respectively.

source	high frequency	low frequency
wavelength	$\lambda = 9$	$\lambda = 50$
Strouhal number	$\mathrm{St} = 4.22$	$\mathrm{St} = 0.76$
convected wavelength	$\lambda_c = 13.5$	$\lambda_c = 75$
wave number	$\tilde{\alpha} = 5.01$	$\tilde{\alpha} = 0.90$

Table 1: Characteristics of the two acoustic sources. The Strouhal number is defined as $\mathrm{St} = (c/\lambda) \times 2\delta/u_{axe}$. The convected length wave is $\lambda_c = (1+M)\lambda$, and the normalized wave number is $\tilde{\alpha} = 2\pi/(\beta\lambda_c)$.

where $\tilde{y}$ is the normalized transverse coordinate, $\tilde{y} = \beta y$ with $\beta = \cosh^{-1}\left(\sqrt{2}\right)/\left(3\sqrt{10}\right) \approx 0.0929$ and $u_{axe} = 0.5$. The value of β is chosen such that the velocity profile (8) collapses to a Gaussian profile $u_o(y) = 0.5e^{-\alpha y^2}$ with $\alpha = \ln(2)/90$. The half-width is then $b = 3\sqrt{10}$. The Bickley profile has an inflexion point at $\tilde{y} = \tanh^{-1}\left(1/\sqrt{3}\right)$, and as a consequence, this profile can be unstable for inviscid linear disturbances.

It is well known that the three modes supported by linearized Euler's equations, namely the acoustic waves, the entropy wave and the vorticity wave, are coupled for a nonuniform mean flow. In particular for the present work, the vorticity mode can be excited by the sound waves and by the acoustic source itself. Drazin & Howard[7] have studied the linear insvicid instability of the Bickley jet (8). A linear velocity fluctuation described by the stream function $\psi(x,y) = \phi(y)\, e^{i\alpha(x-ct)}$ is unstable if the wave number α is such that $0 \leq \alpha \leq 2$ for the even mode (sinuous oscillations) and $0 \leq \alpha \leq 1$ for the odd mode (varicose oscillations); in these cases the wave speed c is written $c = c_r + ic_i$ with a positive imaginary part $c_i > 0$.

Two calculations have been performed for two frequencies of the acoustic source. The first one is a high frequency corresponding to a stable response of the Bickley jet. The second case corresponds to an unstable excitation of the vorticity mode. Table 1 gives the characteristics of the two acoustic sources. The computational domain is rectangular, extending from -200 to 200 in x and in y. Thus, the size of the regular mesh is 400×400 points. The acoustic source is located at $x = -100$ and $y = 0$. All the calculations are performed with a CFL number of 1, without the artificial selective damping. The acoustic source is implemented in the linearized Euler's equations with:

$$\mathrm{S}(x,y) = \epsilon \sin(\omega t)\, e^{-\alpha\left(x^2+y^2\right)} \begin{pmatrix} 1 \\ 0 \\ 0 \\ 1 \end{pmatrix} \quad \text{where} \quad \alpha = \frac{\ln 2}{9} \quad \text{and} \quad \epsilon = 0.01.$$

Figure 8 shows iso-contours of the pressure for the two frequencies. The radiation pattern is strongly modified by the mean flow. The acoustical intensity reaches a peak downstream near the angle θ given by $\cos\theta = 1/(1+M)$. For smaller angles, the intensity decreases due to the refraction effects, and a shadow zone is observed. These results are in agreement with the geometrical approximation valid for high frequencies. A ray tracing is plotted in Figure 9 for the high frequency source. The equations used are given in appendix B. The characteristics of the source radiation are well retrieved,

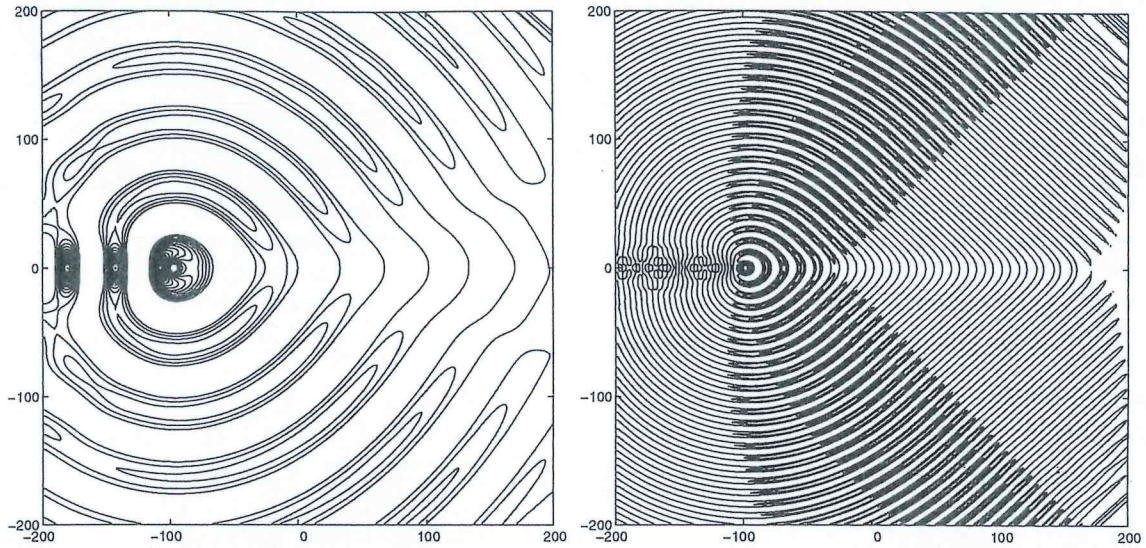

Figure 8: Instantaneous contours of the pressure at time $t = 640$ for the two source frequencies, 21 iso-lines on the [0 ; 0.02] interval.

and the wave fronts have the same oval pattern. The vorticity is displayed in Figure 10 for the two frequencies. As predicted by the linear instability theory, vorticity disturbances appears downstream of the location of the source, and do not decrease for the low frequency acoustic excitation. We can observe vorticity upstream of the source, which is produced by interaction with acoustic waves in the shear zone: this is the only way to get vorticity, because the vorticity fluctuations are necessarily convected by the mean flow. We know[7] for the odd mode the expression of ϕ for the value $\alpha = 1$ of the wave number. This eigenfunction associated with symmetrical oscillations of the velocity is $\phi(y) = \tanh y / \cosh y$. Then the calculation of the vorticity leads to:

$$\omega = \frac{\partial v'}{\partial x} - \frac{\partial u'}{\partial y} = \left[-\frac{d^2\phi}{dy^2} + \alpha^2 \phi \right] e^{i\alpha(x-ct)}$$

which is an odd function of y. In the numerical simulation, the value of the wave number α is close to unity, $\alpha = 0.9$, and the calculated fluctuations of vorticity are an odd function of the tranverse coordinate y too.

7 Concluding remarks

The linearized Euler's equations govern propagation of acoustic fluctuations and the SNGR model provides a means to generate the aeroacoustic sources. This alternative way with respect to a direct numerical simulation for computing the turbulent mixing noise requires a good solver. The combination of the 7-point DRP scheme of Tam & Webb in space with a fourth order Runge-Kutta algorithm in time leads to very good results in terms of accuracy, stability CFL number and low storage. The source radiation in a shear flow shows that CAA allows us to improve our understanding of acoustic – mean flow interaction and to be hopeful about good results for the three-dimensional SNGR model.

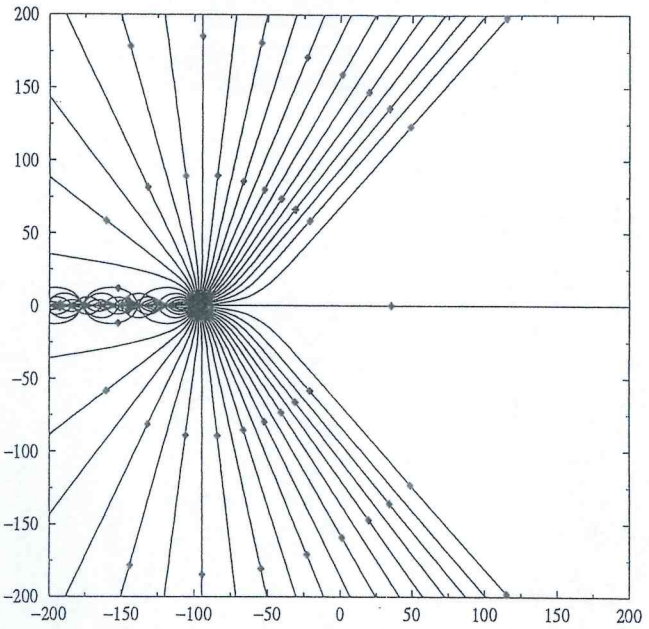

Figure 9: Ray tracing for the high frequency source. The angle of the shadow zone given by $\cos\theta = 1/(1+M)$, that is $\theta \approx 48°$, is well retrieved. The wave fronts are marked by the diamonds.

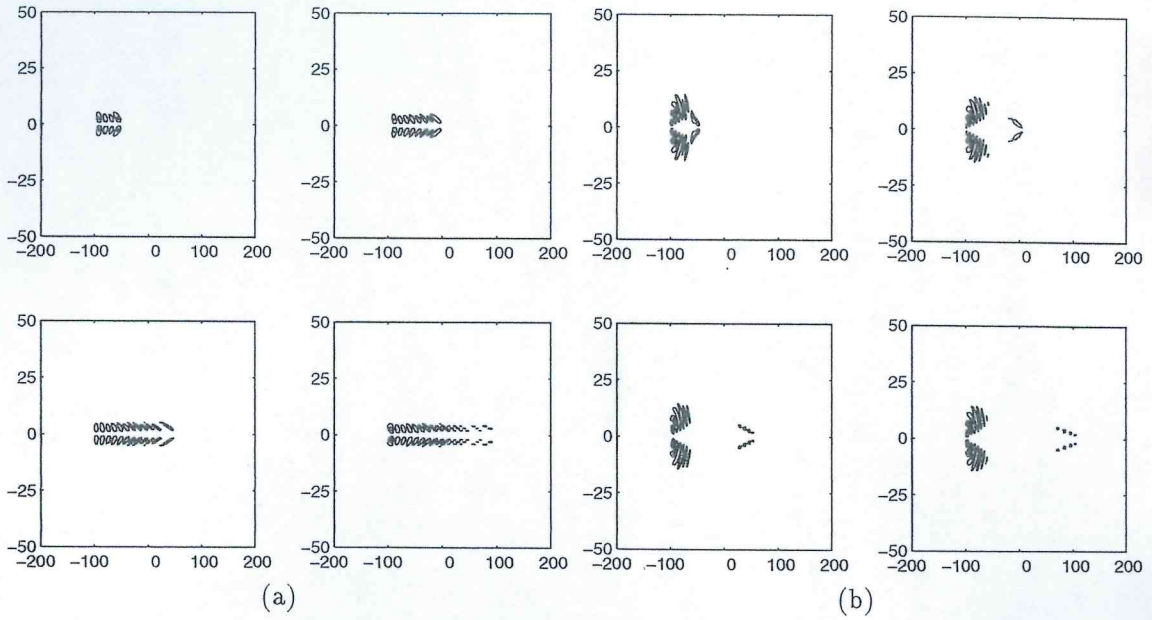

Figure 10: Iso-contours of the vorticity for the low frequency source (a) and for the high frequency source (b) at time $t = 160$, $t = 320$, $t = 480$ and $t = 640$.

Acknowledgments

Computing time was provided by Institut du Développement et des Ressources en Informatique Scientifique (IDRIS). Raphaël Thévenin is a graduate student of Ecole Polytechnique (Palaiseau, France).

References

[1]Bailly, C. 1994, Modélisation du rayonnement acoustique des coulements turbulents libres subsoniques et supersoniques, *Ecole Centrale Paris (France)*, Ph. D., 1994-19.

[2]Bailly, C., Lafon, P. & Candel, S., 1995, A stochastic approach to compute noise generation and radiation of free turbulent flows, AIAA Paper 95-092.

[3]Bailly, C., Lafon, P. & Candel, S., 1996, Computation of noise generation and propagation for free and confined turbulent flows, AIAA Paper 96-1732.

[4]Béchara, W., Bailly, C., Lafon, P. & Candel, S., 1994, Stochastic approach to noise modeling for free turbulent flows, *AIAA Journal*, **32**(3), 455-463.

[5]Candel, S.M., 1977, Numerical solution of conservation equations arising in linear wave theory: application to aeroacoustics, *J. Fluid Mech.*, **83**(3), 465-493.

[6]Comte-Bellot, G., Bailly, C. & Blanc-Benon, P., 1996, Modelling tools for flow noise and sound propagation through turbulence (lecture 6), ed. O. Métais & J. Ferziger, in New tools in turbulence modelling, Les Houches School, May 21-31, *Springer*, France, 141-162.

[7]Drazin, P.G. & Reid, W.H., 1981, Hydrodynamic stability, *Cambridge University Press.*

[8]Hayder, M.E., 1995, An assessment of artificial damping models for aeroacoustic calculations, AIAA Paper 95-2167.

[9]Hu, F.Q., Hussaini, M.Y. & Manthey, J.L., 1996, Low-dissipation and low-dispersion Runge-Kutta schemes for computational acoustics, *J. Comput. Phys.*, **124**, 177-191.

[10]Lafon, P., 1995, Computation of wave propagation in a complex flow, in NASA CP 3300, 125-132.

[11]Lighthill, J., 1978, Waves in fluids, *Cambridge University Press.*

[12]ICASE / NASA, 1995, Workshop on benchmark problems in computational aeroacoustics, NASA CP 3300, edited by Hardin, J.C., Ristorcelli, J.R. & Tam, C.K.W.

[13]Tam, C.K.W. & Webb, J.C., 1993, Dispersion-relation-preserving finite difference schemes for computational acoustics, *J. Comput. Phys.*, **107**, 262-281.